3AF International Conference TSAS
Towards Sustainable Aviation Summit
28-30 January 2025, Toulouse-France

# Exergy-based aerodynamic analysis methodology for low-fidelity aircraft design

Guillaume Bourreau-Tirel *
*Aura Aero, France, guillaume.bourreautirel@aura-aero.com*

Sébastien Duplaa†
*ISAE-SUPAERO, Toulouse University, France, Sebastien.DUPLAA@isae.fr*

Miguel Angel Aguirre‡
*Aura Aero, France, miguelangel.aguirre@aura-aero.com*

**Aerodynamic analysis based on the exergy method provides a drag breakdown assessment which can become a particularly valuable design tool for developing innovative, low-carbon-impact aircraft with improved fuel efficiency. Until now, the existing exergy formulations are appropriate for mid-fidelity data such as RANS computation results, as well as wind tunnel testing data. However, the preliminary aircraft design phases in the industry massively use low-fidelity modeling such as panel method solvers with viscous coupling since they require far fewer computing resources than mid-fidelity RANS simulations. A new exergy-based analysis formulation for profile drag, suited to low-fidelity data, is introduced, linking exergy terms with boundary layer integral quantities. This low-fidelity, exergy-based aerodynamic analysis formulation has been validated through comparison with existing mid-fidelity exergy formulations for the flat plate test case.**

## I. Nomenclature

| | | |
|---|---|---|
| $\dot{\mathcal{A}}$ | = | total anergy, W |
| $b, c$ | = | wingspan and chord, m |
| $c_{\mathcal{D}}$ | = | dissipation coefficient |
| $c_f$ | = | skin friction coefficient |
| $C_D$ | = | drag coefficient |
| $\dot{E}_u$ | = | axial kinetic exergy, W |
| $\dot{E}_v$ | = | transverse kinetic exergy, W |
| $\dot{E}_p$ | = | pressure exergy, W |
| $M$ | = | Mach number |
| $H$ | = | $\frac{\delta^*}{\theta}$ boundary layer shape factor |
| $\hat{\mathbf{n}}$ | = | local surface normal |
| $P_S$ | = | static pressure, Pa |
| $Pr$ | = | Prandtl number |
| $r$ | = | temperature revovery parameter $\sqrt{Pr}$ |
| $R_e$ | = | Reynolds number |
| $\mathfrak{s}$ | = | mass spectific entropy, $\mathrm{J \cdot kg^{-1} \cdot K^{-1}}$ |
| $S$ | = | surface, $\mathrm{m^2}$ |
| $s, n$ | = | local boundary layer axes |
| $T_S$ | = | static temperature, K |
| $U, V$ | = | local boundary layer velocity components, $\mathrm{m \cdot s^{-1}}$ |
| $u, v, w$ | = | velocity components in aerodynamic frame, $\mathrm{m \cdot s^{-1}}$ |
| $\mathbf{V}$ | = | local velocity vector, $\mathrm{m \cdot s^{-1}}$ |
| $x, y, z$ | = | aerodynamic axes, m |
| $\gamma$ | = | ratio of specific heats |
| $\dot{\varepsilon}_m$ | = | mechanical exergy, W |
| $\dot{\varepsilon}_{th}$ | = | thermal exergy, W |
| $\delta$ | = | boundary layer thickness, m |
| $\theta, \delta^*$ | = | momentum and displacement thicknesses, m |
| $\theta^*, \delta^{**}$ | = | kinetic energy and density-flux thicknesses, m |
| $\rho$ | = | fluid density, $\mathrm{kg \cdot m^{-3}}$ |
| $\bar{\bar{\tau}}$ | = | shear stress tensor, Pa |

*Subscripts*

| | | |
|---|---|---|
| 0 | = | freestream quantity |
| $e$ | = | boundary layer edge quantity |
| $out$ | = | outlet section |
| $p$ | = | profile drag |
| $ref$ | = | reference value |
| $\varepsilon$ | = | exergy-based value |

*Superscripts*

| | | |
|---|---|---|
| $*$ | = | isentropic (inviscid) component |
| $\overline{()}$ | = | non-isentropic (viscous) component |

*Ph.D. Candidate, Aura Aero/ISAE-Supaéro.
†Associate Professor, DAEP-Department of Aerodynamics, Energetics and Propulsion.
‡Aerodynamics Manager, Aura Aero.

## II. Introduction

The current state of the aeronautics industry, driven by the goal of achieving carbon neutrality in aviation, presents both new challenges and opportunities in aircraft design. A key trend is the evolution towards the development of electrically propelled aircraft, featuring more integrated propulsion systems and a focus on advanced aero-thermal management. This evolution is giving rise to new, disruptive aircraft architectures, characterized by tightly coupled geometries and complex aero-propulsive interactions that can no longer be effectively analyzed using the traditional “tube-and-wing” model, which relies on simple thrust-drag accounting.

By comparing the work actually exploited by a system against the maximum work allowed by a Carnot cycle with an efficiency lower than unity, exergy analysis allows quantifying the margin of improvement. The aerodynamic exergy analysis method, which combines the principles of energy and thermodynamics, therefore offers a promising alternative for assessing performance of these innovative aircraft designs. Currently, existing exergy analysis methods are well-suited for use with data from mid-fidelity computational methods or wind tunnel testing.

The limitation arises from the significant computational demands of mid-fidelity simulation which limit their application in the early design phases and time-critical scenarios, for the estimation of aerodynamic loads across multiple flight conditions and design variations. As a result, the industry largely uses low-fidelity modeling such as panel method solver with viscous coupling since they require far fewer computing resources than mid-fidelity simulations to deliver flow field predictions across the entire flight envelope. There is therefore a clear need to develop an exergy formulation suited to low-fidelity simulation data, enabling rapid evaluation of complex aircraft configurations during the preliminary design phase. The current work outlines the key concepts of the methodology used to create a low-fidelity version of exergy-based aerodynamic analysis. The principles of the low-fidelity computations and the power-based aerodynamic analysis methods are presented to emphasize the link between exergy and integral boundary layer quantities. An analytical expression for the exergy associated with profile drag is derived and validated using the flat plate case.

## III. Low-fidelity and boundary layer modeling

It is important to clearly distinguish between mid-fidelity and low-fidelity calculation methods :

- Mid-fidelity simulations involve a mesh that covers the entire spatial domain around the body. This approach, shown on the left of Fig.1, is used by CFD software to solve RANS (Reynolds-Average-Navier-Stokes) equations. While these simulations are accurate and robust, they require relatively high computational resources. Indeed,$\mathbf{V}$ and shear-stress tensor $\bar{\bar{\tau}}$ must be resolved at each mesh node . The term "mid-fidelity" refers to the fact that these RANS simulations require a turbulent viscosity model as a closure relation for the Navier-Stokes equations.
- On the other hand, low-fidelity simulations do not require meshing the entire flow field. Instead, they model the perturbations in the potential inviscid flow field by applying singularities (such as sources $\lambda_i$ or vortex $\gamma_i$ sheets) at the body surface. This approach, presented on the right of Fig.1, requires far fewer computational resources than the previous one, as only the body surface is discretized in panels. This is why low-fidelity panel methods are widely used in the aeronautical industry for large-scale study campaigns, particularly in cases where high-fidelity simulations would be prohibitively expensive in computational resources.

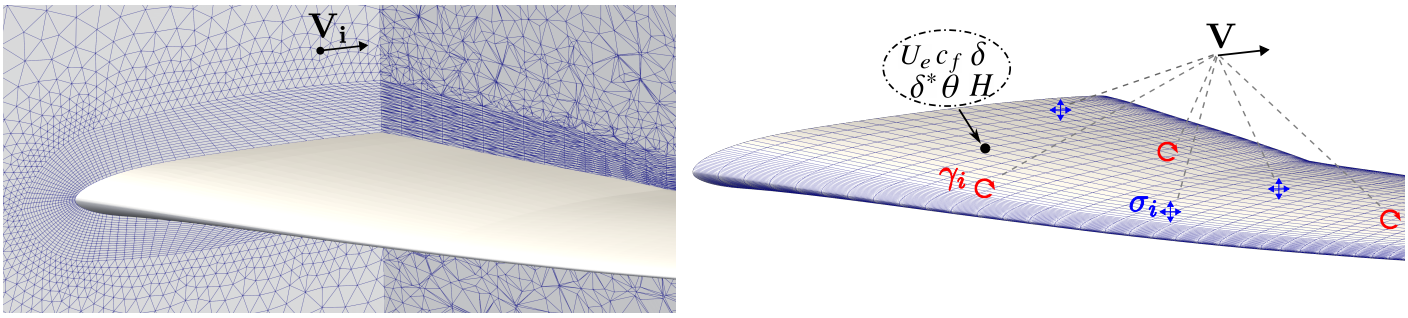



**Fig. 1 Comparison of mid-fidelity (left) and low-fidelity (right) approaches**

In low-fidelity computational methods, viscous effects contributing to the profile drag component are modeled through a viscous coupling procedure. This involves an iterative correction process of the singularity distribution on the body surface mesh, which accounts for the displacement effect of the boundary layer. The inviscid flow solution, based on the singularity distribution at the body surface, is thus coupled with the boundary layer solution. A lumped representation of the boundary layer is employed, modeling it using quantities integrated across its thickness $\delta$. At each surface mesh node of the panel solver, the boundary layer description is reduced to a few representative scalar quantities (such as $\delta$, skin friction coefficient $c_f$, boundary layer displacement thickness $\delta^*$, momentum thickness $\theta$ or shape factor $H$, see [1]), rather than the detailed velocity profile across the boundary layer domain. This simplified representation of the boundary layer represented in Fig.2 is particularly well-suited for low-fidelity viscous coupling computations due to its low computational cost. The primary governing equation for this lumped boundary layer approach is the so-called "von Kármán equation" given by Eq.1. Here, $U_e$ and $M_e$ represent respectively the tangent velocity and Mach number at the edge of the boundary

layer, that is, at $n = \delta$. For the remainder of the paper we define $x$, $y$, $z$ as the traditional aerodynamic axes, while $s$ and $n$ correspond to the local boundary layer coordinates, with $s$ lying along the body surface and $n$ to it (as shown in Fig.2). Also, $u$, $v$, $w$ will denote the velocity components along the $x$, $y$ and $z$ axes respectively, while $U$, $V$ refer to the velocity components along the $s$ and $n$ directions.

$$\boxed{\frac{\mathrm{d}\theta}{\mathrm{d}s} = \frac{c_f}{2} - \left(H + 2 - M_e^2\right)\frac{\theta}{U_e}\frac{\mathrm{d}U_e}{\mathrm{d}s}} \tag{1}$$

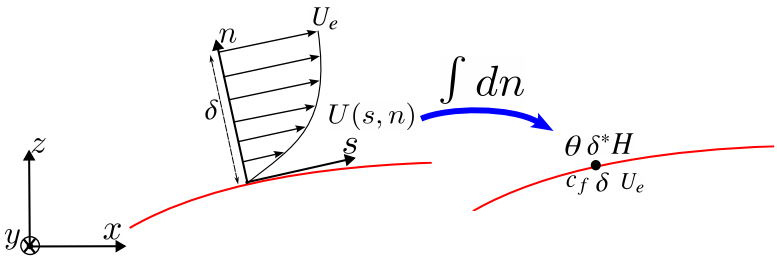



**Fig. 2 Integral description of the boundary layer**

The outputs of the viscous coupling process for low-fidelity simulations include the edge velocity $U_e$ and Mach number $M_e$ obtained from the singularity surface distribution around the body as well as the integral parameters $c_f$, $\delta$ $\theta$ and $H$ used to represent boundary layer viscous effect and computed by solving the von Kármán equation Eq.1 and an additional equation for two-equations models (see [2], [3], [4]).

## IV. Review of Power-based aerodynamic assessment methods

### A. Power balance

The power balance formulation introduced in 2009 by Drela [5] marked a major breakthrough in aerodynamic analysis. Thus, while far-field methods for assessing drag and lift (Betz [6], Maskell [7], Kusunose [8], Meheut [9]) are based on a momentum equation analysis, the power balance method relies on mechanical energy considerations, which do not require a decomposition of forces into thrust and drag contributions. The power balance method, instead, establishes a relation between power sources and sinks in the flow field, making it particularly suited for studying complex geometries, especially those with integrated propulsion configurations where thrust-drag bookkeeping is ambiguous.

The power balance equations are derived from the dot product of the Navier-Stokes momentum conservation equation and the velocity, which gives the conservation of kinetic energy of Eq.2:

$$\nabla \cdot (\rho \mathbf{V} \frac{\mathbf{1}}{\mathbf{2}} \mathbf{V^2}) = -\nabla P_S \cdot \mathbf{V} + (\nabla \cdot \bar{\bar{\tau}}) \cdot \mathbf{V} \tag{2}$$

Integrating the latter within the control volume shown in Fig.3 yields the following scalar mechanical power balance equation:

$$\boxed{P_S + P_K + P_V = W\dot{\Gamma} + \dot{E}_u + \dot{E}_v + \dot{E}_p + \dot{E}_w + \dot{E}_\Phi} \tag{3}$$

The terms on the left side of Eq.3 represent power sources: $P_S$ and $P_K$ correspond to mechanical power production, while $P_V$ accounts for thermal power added to the system. On the right side of the power balance equation, $W\dot{\Gamma}$ represents the aircraft potential energy rate (the aircraft's energy accumulation capacity), $\dot{E}_u$, $\dot{E}_v$ and $\dot{E}_p$ are respectively the wake streamwise kinetic energy, transverse kinetic energy and pressure-defect work rates crossing the survey plane, $\dot{E}_w$ is the power dissipated through shock waves, and $\dot{E}_\Phi$ is the power associated with viscous dissipation within the control volume.

In his PhD thesis, Sato [10] develops a kind of "shear layer-reduced" version of the power balance of Drela, using the mechanical energy steady boundary layer equation 4 to derive an analytical expression of profile drag. By using the integral boundary layer kinetic energy equation 4 instead of the kinetic energy equation 2, Sato actually performs a low-fidelity adaptation of the power balance of Drela. The latter, described through Eq.3 with the associated control volume depicted in Fig.3, is presented from a far-field viewpoint well-suited to mid-fidelity simulations like RANS but not to low-fidelity models. Indeed, to compute the wake quantities of Drela $\dot{E}_u$, $\dot{E}_v$ and $\dot{E}_p$ obtained by integration over the entire survey plane surface, it is necessary to know the detailed velocity profile along this plane. This is typically provided by a mid-fidelity simulation, where the velocity field is calculated at each mesh point around the object. However, such information is not available with a low-fidelity simulation, which only provides integral boundary layer parameters at the surface of the body as described in the previous section III.

The quantities $K$, $\mathcal{D}$ in Eq.5, obtained by integration exclusively performed over the boundary layer thickness $\delta$, can respectively be interpreted as the "shear layer-reduced" counterparts of quantities $\dot{E}_u$ and $\dot{E}_\Phi$ of Eq.1. This is how Sato performs a lumping of the power balance formulation to the shear-layer domain (boundary layer + wake). $K$ represents the kinetic energy defect within the boundary layer (related to the kinetic energy thickness $\theta^*$). $\mathcal{D}$, known as the dissipation integral and associated to its non-dimensional coefficient $c_\mathcal{D}$, quantifies the kinetic energy dissipation caused by viscosity. The remaining term linking $D$ to $\frac{\mathrm{d}U_e}{\mathrm{d}s}$ is referred to as

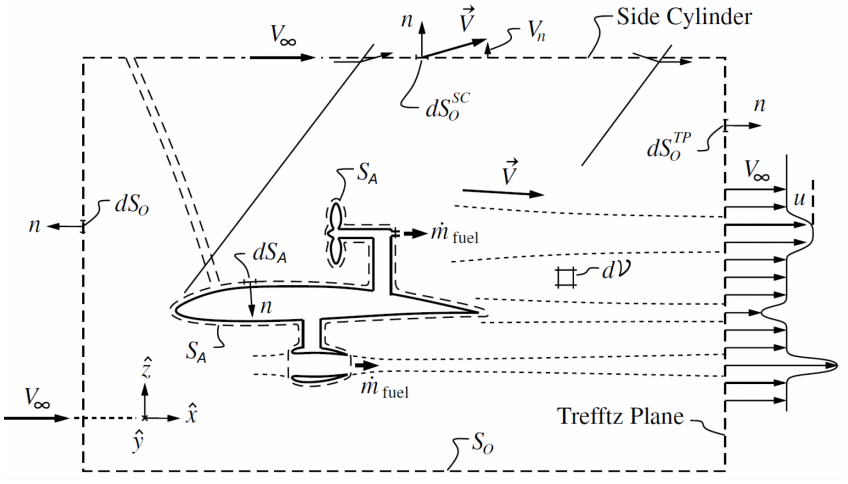



**Fig. 3 Power balance method: definition of the control volume, adapted from [5]**

"baroclinic power" and measures the work done by the pressure gradient in conjunction with density variations across the boundary layer.

$$\frac{\mathrm{d}K}{\mathrm{d}s} = \mathcal{D} - D\,U_e\frac{\mathrm{d}U_e}{\mathrm{d}s} \tag{4}$$

$$K = \frac{1}{2}\rho_e U_e^3\theta^* = \frac{1}{2}\int_0^\delta \left(U_e^2 - U^2\right)\rho U\,dn \qquad D = \rho_e U_e \delta^{**} = \int_0^\delta (\rho_e - \rho)\,U\,dn \qquad \mathcal{D} = \rho_e U_e^3 c_{\mathcal{D}} = \int_0^\delta (\bar{\bar{\tau}}\cdot\nabla)\cdot U\,dn \tag{5}$$

The dimensionless form of Eq.4 is given by Eq.6 which is the energy-based equivalent of the von Kàrmàn integral momentum equation Eq.1 used for viscous coupling in low-fidelity simulation as presented in the previous section III.

$$\frac{\mathrm{d}\theta^*}{\mathrm{d}s} = 2c_{\mathcal{D}} - \left(2\frac{\delta^{**}}{\theta^*} + 3 - M_e^2\right)\frac{\theta^*}{U_e}\frac{\mathrm{d}U_e}{\mathrm{d}s} \tag{6}$$

By integrating Eq.6 over the boundary layer and wake domains shown in the left part Fig.4, Sato proposes an analytical expression for the profile drag coefficient $C_{D_p}$(Eq.7) which depends exclusively on boundary layer integral quantities.

$$C_{D_p} = \frac{\iint_{S_{BL}+S_{wake}} \rho_e U_e^3 (1+\frac{\gamma-1}{2}M_e^2)^r c_{\mathcal{D}}\,dS}{\frac{1}{2}\rho_0 u_0^3\ (1+\frac{\gamma-1}{2}M_e^2)^r|_{out}} \tag{7}$$

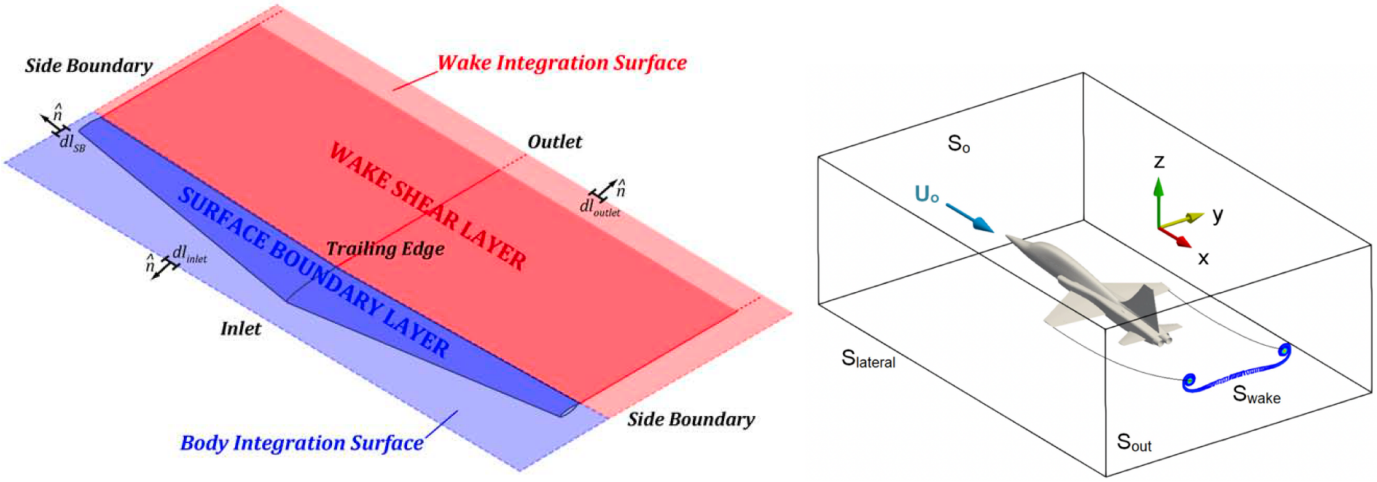



**Fig. 4 Left: Integration domain used by Sato (boundary layer + wake) adapted from [10], right: control volume used for exergy analysis by Arntz and Aguirre adapted from [11]**

### B. Exergy

Exergy is a thermodynamic quantity derived from the breakdown of the total energy of a system provided by the first and second law of thermodynamics. Thus, the second law of thermodynamics allows distinguishing the maximum fraction of work that could be obtained by bringing back the system to the thermodynamic equilibrium following a reversible transformation (ie a Carnot cycle with an efficiency lower than unity). This is the definition of exergy, which is theoretically fully convertible into mechanical work and therefore referred to as the "useful" part of energy. On the other hand, anergy corresponds to the "useless" work, which cannot be converted back into mechanical work. Anergy is related to irreversibilities and, thus, to entropy generation.

In 2014, Arntz [12] developed a reliable and accurate exergy-based aerodynamic analysis method suited to mid-fidelity RANS simulation data. Like the power balance of Drela, Arntz's formulation is presented for a far-field viewpoint with quantities evaluated at a survey plane $S_{out}$ placed downstream of the body as shown on the right side of Fig.4.
Arntz's exergy balance of Eq.8 is derived from the combination of mass and momentum conservation equations with the first and second laws of thermodynamics, then integrated over the control volume defined on the right side of Fig.4.

$$\boxed{\dot{\varepsilon}_{prop} + \dot{\varepsilon}_q = W\dot{\Gamma} + \dot{\varepsilon}_m + \dot{\varepsilon}_{th} + \dot{\mathcal{A}}} \tag{8}$$

Similarly to Eq.3, the left side of Eq 8 gathers terms related to exergy supplied to the system either by the propulsion devices with $\dot{\varepsilon}_{prop}$ or by heat transfer with $\dot{\varepsilon}_q$. $W\dot{\Gamma}$ is the aircraft capacity of accumulation of exergy similarly to the term found in Eq 3. $\dot{\varepsilon}_m$ is the mechanical exergy that flows out of the domain through $S_{out}$ and can be decomposed into an axial $\dot{E}_u$ and transverse $\dot{E}_v$ kinetic exergy components and a pressure exergy term $\dot{E}_p$.

$$\dot{\varepsilon}_m = \dot{E}_u + \dot{E}_v + \dot{E}_p \tag{9}$$

$$\dot{E}_u = \int_{S_{out}} \frac{1}{2}\rho(u-u_0)^2(\mathbf{V}\cdot\hat{\mathbf{n}})dS \tag{10}$$

$$\dot{E}_v = \int_{S_{out}} \frac{1}{2}\rho(v^2+w^2)(\mathbf{V}\cdot\hat{\mathbf{n}})dS \tag{11}$$

$$\dot{E}_p = \int_{S_{out}} \frac{1}{2}(P_S - P_{S_0})[(\mathbf{V}-\mathbf{V}_0)\cdot\hat{\mathbf{n}}]dS \tag{12}$$

The thermal exergy $\dot{\varepsilon}_{th}$ is related to the temperature perturbation and can be considered negligible in the adiabatic case.
Anergy $\dot{\mathcal{A}}$ as a result of irreversibilities is directly linked with the entropy generation $\delta\mathfrak{z}$ across the survey plane as described by Eq.13

$$\dot{\mathcal{A}} = T_{S_0}\int_{S_{out}} \rho\ \delta\mathfrak{z}\ (\mathbf{V}\cdot\hat{\mathbf{n}})\ dS \tag{13}$$

The Arntz formulation introduces the so-called "exergy-based drag coefficient" (Eq.14), which applies to the unpowered case. It allows for a breakdown of drag into two components: one that is potentially recoverable (the exergy terms $\dot{\varepsilon}_m$ and $\dot{\varepsilon}_{th}$), and the other that is lost due to irreversibilities (the anergy $\dot{\mathcal{A}}$).

$$C_{D_\varepsilon} = \frac{\dot{\varepsilon}_m + \dot{\varepsilon}_{th} + \dot{\mathcal{A}}}{\frac{1}{2}\rho_0 u_0^3 S_{ref}} \tag{14}$$

Aguirre [13][11] recently proposed a wake-reduced formulation, based on the Arntz approach, aimed at developing a suitable method for wind tunnel experimental data. Indeed, while Arntz's equations for exergy and anergy estimations require integration over the entire survey plane surface ($S_{out}$ on right side of Fig.4), Aguirre's method simplifies this by reducing the integration to the much more confined wake surface ($S_{wake}$ on right side of Fig.4). The key idea behind Aguirre's development is the decomposition of the velocity field into its isentropic ($u^*$) and non-isentropic ($\overline{u}$) components (Eq.15). Outside the viscous region, the velocity components are entirely isentropic, as a fluid particle follows a purely isentropic process along the streamline. However, within the viscous regions (boundary layer and wake), the particle undergoes a non-isentropic process along its path, so the local velocity components consist of both isentropic and non-isentropic contributions.

$$\mathbf{V} = \mathbf{V}^* + \overline{\mathbf{V}} \tag{15}$$

Here, the isentropic velocity vector $\mathbf{V}^*$ is linked to the equivalent pure isentropic flow, also known as the Equivalent Inviscid Flow (EIF), as described by Drela [14]. This isentropic velocity represents the strictly fictitious potential flow, which can be obtained, for example, using a panel method without viscous coupling. This is illustrated in Fig.5, where the isentropic field $V^*$ captures the pure potential effects around the airfoil, including the local velocity variations induced by the velocity-pressure coupling described by the Bernoulli equation. It excludes all non-isentropic phenomena, such as the boundary layer and wake regions, where irreversibilities arise due to viscous dissipation.

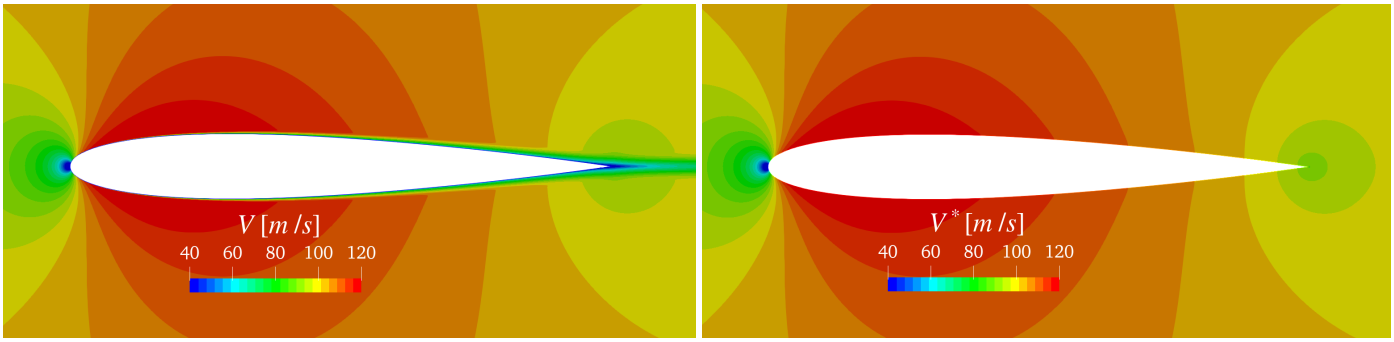



**Fig. 5 Real (left) and isentropic (right) velocity magnitude fields** ($\alpha = 0°$, **Mach=0.3**)

Aguirre's velocity decomposition, along with the corresponding decomposition of the density field $\rho$ and static temperature $T_S$ into isentropic and non-isentropic components, enables the breakdown of the Arntz exergy quantities (Eq.9 to 12) into their isentropic and non-isentropic components (Eq.16).

$$\dot{E}_u = \dot{E}^*_u + \overline{\dot{E}}_u \qquad \dot{E}_v = \dot{E}^*_v + \overline{\dot{E}}_v \qquad \dot{E}_p = \dot{E}^*_p + \overline{\dot{E}}_p \qquad \dot{\varepsilon}_m = \dot{\varepsilon}^*_m + \overline{\dot{\varepsilon}}_m \qquad \dot{\varepsilon}_{th} = \dot{\varepsilon}^*_{th} + \overline{\dot{\varepsilon}}_{th} \tag{16}$$

Aguirre demonstrates that for steady-state, non-lifting bodies, the non-isentropic mechanical exergy $\overline{\dot{\varepsilon}}_m$ is the net exergy with recovery potential, and it is the one that should be observed when analyzing the flow field.

The interesting property of non-isentropic exergy, as illustrated by $\overline{\dot{\varepsilon}}_m$ in Fig.6, is that it is non-zero in the shear-layer region (boundary layer and wake) hence the denomination "wake-reduced". In a sense, Aguirre provides the first step toward adapting the exergy formulation of Arntz to the shear-layer domain, similar to what Sato did for the power balance of Drela.

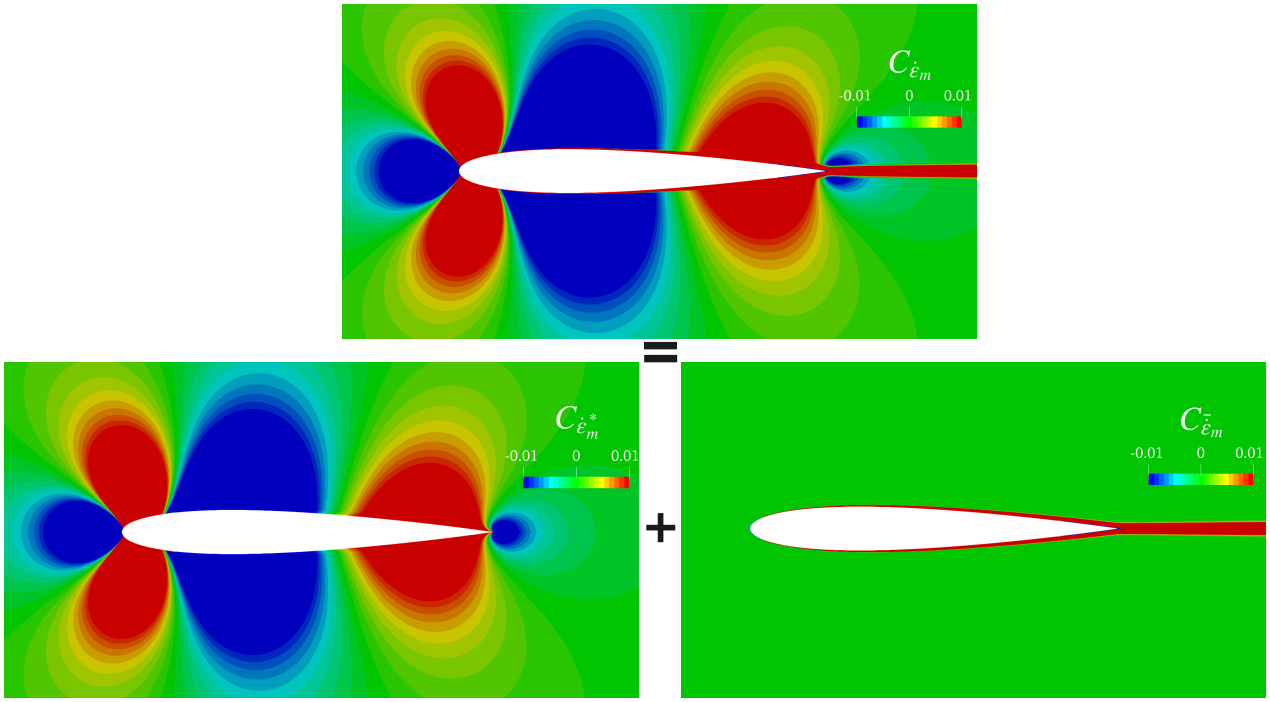



**Fig. 6 Total mechanical exergy fields (top) breakdown into its isentropic (bottom left) and non-isentropic (bottom right) components** ($\alpha = 0°$, **Mach=0.3**)

Finally, Aguirre proposes a drag decomposition (Eq.17,19 and 18) of Arntz's drag expression (Eq.14) splitting it into isentropic $C_{D^*_\varepsilon}$ and non-isentropic $C_{\overline{D}_\varepsilon}$ components. Here, $C_{D^*_\varepsilon}$ gives the vortex drag and is not wake-reduced and $C_{\overline{D}_\varepsilon}$ gives the profile drag and is wake-reduced. Indeed, non-isentropic exergies $\overline{\dot{\varepsilon}}_m$ and $\overline{\dot{\varepsilon}}_{th}$ are wake-reduced, as explained above, along with the anergy $\dot{\mathcal{A}}$ which is, by definition, linked to entropy generation only taking place in boundary layer and wake regions.

$$C_{D_\varepsilon} = C_{D^*_\varepsilon} + C_{\overline{D}_\varepsilon} \tag{17}$$

$$C_{D_\varepsilon^*} = \frac{\dot{\varepsilon}_m^* + \dot{\varepsilon}_{th}^*}{\frac{1}{2}\,\rho_0 u_0^3\, S_{ref}} \tag{18}$$

$$C_{\overline{D}_\varepsilon} = C_{D_p} = \frac{\overline{\dot{\varepsilon}}_m + \overline{\dot{\varepsilon}}_{th} + \dot{\mathcal{A}}}{\frac{1}{2}\,\rho_0 u_0^3\, S_{ref}} \tag{19}$$

The summary of profile drag expressions corresponding to power balance and exergy methods is given in Table 1.

| Method : | Sato (2012) | Arntz (2014) | Aguirre (2022) | Current work |
|---|---|---|---|---|
| Type of analysis : | power balance | exergy | exergy | exergy |
| Shear layer-reduced : | yes | no | yes for profile drag | yes |
| Input data Suitability: | panel method | RANS | RANS and WTT | panel method |
| Drag expression: | profile drag Eq.7 | total drag Eq.14 | profile and vortex drag Eq.18,19 | **?** |

**Table 1 Overview of power-based aerodynamic analysis methods**

## V. Low-fidelity formulation for $\overline{\dot{E}}_u$

### A. $\overline{\dot{E}}_u$ link with BL quantities

The first step in developing the low-fidelity formulation addresses the non-isentropic mechanical exergy $\overline{\dot{\varepsilon}}_m$. $\overline{\dot{\varepsilon}}_m$ is the component of profile drag that represents the mechanical exergy that can actually be recovered, and directly quantifies the "margin for improvement" of a given geometry, which is highly useful for design purposes. Here, we focus on the axial component $\overline{\dot{E}}u$ of $\overline{\dot{\varepsilon}}m$ because, in the case of a flat plate (with no pressure gradient), where the aerodynamic and local boundary layer axes coincide, $\overline{\dot{\varepsilon}}m$ is reduced to the term $\overline{\dot{E}}u$. In his formulation, Aguirre calculates this quantity in an 'indirect' manner by subtracting the isentropic mechanical component from the total mechanical exergy term: $\overline{\dot{E}}_u = \dot{E}_u - \dot{E}_u^*$. The key idea behind the development of the exergy-based formulation, suited to low-fidelity data, is to express $\overline{\dot{E}}_u$ (which is confined to the boundary layer region as demonstrated by Aguirre) directly in terms of boundary layer integral quantities. Under the thin boundary layer approximation, an equation for $\overline{\dot{E}}_u$ is derived for the flat plate case by developing the terms $\dot{E}_u - \dot{E}_u^*$ (Eq.20). This expression directly relates $\overline{\dot{E}}_u$ to the integral boundary layer parameters $K$ and $M$ which are associated with the classical energy and displacement boundary layer thicknesses $\theta^*$ and $\delta^*$ respectively. The other boundary layer integral quantities $k$ and $m$, which appear in Eq.20, measure the kinetic energy defect and the mass defect within the boundary layer. Here, $U_e$ is the classical boundary layer edge velocity, an output of the low-fidelity computation, while $u_0$ denotes the freestream velocity. This equation is valid for unpowered flat plate configurations with adiabatic walls.

$$\boxed{\overline{\dot{E}}_u = u_0(k + m\,{U_e}^2) - K - \frac{({U_e}^2 + u_0^2)}{2}M} \tag{20}$$

$$\begin{aligned} k &= \int_0^\delta (U_e^2 - U^2)\,\rho\, dn \qquad & m &= \int_0^\delta (\rho_e - \rho)\, dn \\ K &= \frac{1}{2}\rho_e U_e^3 \theta^* = \frac{1}{2}\int_0^\delta (U_e^2 - U^2)\,\rho U\, dn \qquad & M &= \rho_e U_e \delta^* = \int_0^\delta (\rho_e U_e - \rho U)\, dn \end{aligned} \tag{21}$$

The equation Eq.20 provides an evaluation of the maximum theoretical power that can be recovered along the chord, based on boundary layer integral quantities. This is a particularly valuable tool for design purposes, as it helps assess the profile drag reduction potential of a given geometry. While Sato's low-fidelity power balance formulation only estimates the total profile drag by summing the mechanical power dissipated along the boundary layer and wake region using $c_{\mathcal{D}}$, this low-fidelity exergy equation offers a detailed mapping of potential power-saving opportunities at the surface of the studied body.

In the compressible case, the density profile varies along the boundary layer. Knowing this density profile is essential for correctly evaluating the integral quantities $k$, $m$, $K$ and $M$. However, the Swafford method, described in the next section and used in this study, only allows for the reconstruction of velocity fields from $\theta$ and $H$. Therefore, a relationship is needed to express the density profile $\rho(n)$ as a function of the velocity profile $U(n)$. Under the following assumptions: adiabatic walls, near-unity Prandtl number (which is the case for air, with ($Pr \approx 0.71$) and small flow acceleration ($\frac{d|U_e|}{ds}\frac{c}{V_\infty} \ll 1$), the density profile can be expressed using the Crocco-Busemann relation given by Eq.22. Here, $r$ is the recovery factor expressed as the square of the Prandtl number. This relation is also employed by Whitfield [15] and Sato [10].

$$\frac{\rho_e}{\rho} = \frac{T_S}{T_{S_e}} = 1 + r\frac{(\gamma-1)}{2}M_e^2\left(1 - \frac{U^2}{U_e^2}\right) \qquad r = \sqrt{Pr} \tag{22}$$

### B. Boundary layer profile reconstruction

The analytical equation Eq.20 requires knowledge of the boundary layer integral parameters $k$, $m$, $K$, $M$ along with $U_e$ at each surface node along the body surface.

As mentioned earlier, most low-fidelity software typically provides $U_e$ and boundary layer integral parameters $c_f$, $\delta$, $\delta^*$, $\theta$ and $H$ as a result of their viscous coupling procedure but do not compute $k$ $m$ and $K$ quantities. Since these parameters are not directly available from low-fidelity data, a "reconstruction" of the detailed velocity profile $U(n)$ is required to compute them and to calculate $\overline{\dot{E}}_u$ using Eq.20. This reconstruction procedure therefore consists of retrieving a detailed boundary layer velocity profile $U(n)$ from the integral boundary layer quantities provided by the low-fidelity simulation.

Several semi-empirical methods for computing turbulent velocity profiles are found in the literature, such as those by Coles [16], Whitfield [15] or Swafford [17]. These methods describe the velocity profiles using a composite function (law of the wall), which consists of an inner law for the boundary layer close to the wall and an outer law for the external region. Swafford's method is an extension of Whitfield's, incorporating the possibility of separated velocity profiles. In the incompressible case, the Swafford analytical function describing the turbulent velocity profile is given by Eq.23. The quantities with the '+' superscript are scaled to be adapted to the boundary layer description (see [1]). The first term of this law of the wall describes the inner region of the boundary layer with the sign of $S$, which can take a value of $-1$ when $c_f$ is negative, allowing for the representation of separated flow with local reverse flow near the wall. The second term of the law describes the outer region of the boundary layer with its shape controlled by the constants $a$ and $b$.

$$
\begin{aligned}
U^+ &= \frac{S}{0.09} tanh^{-1}[0.09 n^+] \;+\; (U_e^+ - \frac{8\pi}{0.18}) tanh^{\frac{1}{2}}[a(\frac{n}{\theta})^b] \\
\frac{U}{U_e} &= \frac{U^+}{U_e^+} \qquad U_e^+ = (\frac{2}{c_f})^{\frac{1}{2}} \qquad n^+ = \frac{R_{e\theta}\, n}{U_e^+\, \theta} \qquad S = \frac{c_f}{|c_f|}
\end{aligned}
\tag{23}
$$

The inputs required by the Swafford method to compute the velocity profile according to Eq.23 are $U_e$ and the integral parameters $H$ and $\theta$ all of which are directly provided by the low-fidelity solution. The remaining three unknowns in Eq.23, namely $c_f$, $a$ and $b$ are determined using correlations laws based on experimental measurements as functions of $H$ and $\theta$. The reconstruction method of Swafford has been implemented for the purpose of this study. An example of the resulting turbulent velocity profiles for different shape factors $H$ at a fixed value of $\theta$ is illustrated in Fig.7.

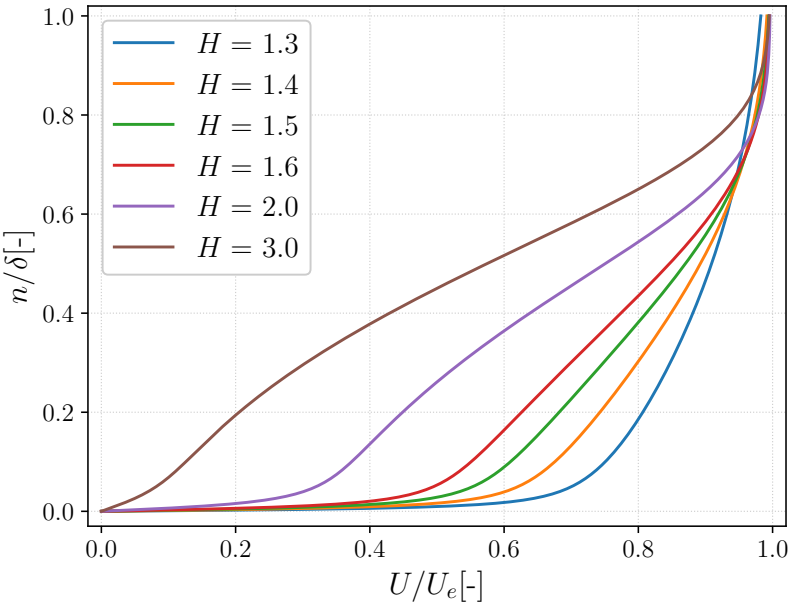



**Fig. 7 Turbulent boundary layer velocity profiles computed with the Swafford method for $Re_\theta$=5000**

## VI. Test case : flat plate

The selected test case for validating the low-fidelity formulation of the non-isentropic axial exergy, $\overline{\dot{E}}_u$, is a 2D flat plate in the turbulent regime. The goal is to generate both mid-fidelity and low-fidelity data for this flat plate case, enabling a comparison between the exergy computed using Aguirre's mid-fidelity formulation and that calculated with the new low-fidelity formulation from Eq.20.

### A. Mid and low fidelity data generation

The 2D fully turbulent smooth flat plate case of length $c = 0.452$m was studied at zero angle of attack, at a Reynolds number of $3 \times 10^6$ and Mach number of 0.3.

The mid-fidelity data are generated from a RANS simulation conducted using the CFD software Ansys Fluent.

The mid-fidelity geometry consists of an infinitely thin flat plate with sharp leading and trailing edges as depicted on the left of Fig.8. A 2D mesh of the flat plate is generated using a symmetry condition, as the upper and lower surfaces exhibit identical flow characteristics. The computational domain extends 46 chord lengths in all directions. A multiblock mesh strategy is employed, with refined boundary layer and wake zones to accurately capture the strong local flow gradients. The mesh includes 200 nodes along the chord, with a wall-normal $y^+$ value of approximately 1, and a maximum growth rate of 1.05 for the mesh refinement. The turbulent RANS simulation is performed with the Spalart-Allmaras turbulence model.

The low-fidelity data are obtained using the panel method solver FlightStream. FlightStream provides 3D potential flow solutions by solving for a linearly varying surface vorticity singularities distribution coupled with a viscous coupling procedure to model the boundary layer effect as described in section III. It is an appropriate tool for performing low-fidelity, exergy-based aerodynamic analyses of unconventional configurations. The low-fidelity geometry shown on the left side of Fig.8 consists of an infinitely thin flat plate with a very large aspect ratio of 80, ensuring that the flow field at $y = 0$ can be considered as corresponding to a 2D configuration. The body surface structured mesh includes 200 nodes along the chord. Viscous coupling for the turbulent regime is achieved using the Standen model [2].

The generated data was analyzed using ParaView and Epsilon, an open source plugin developed by ISAE-SUPAERO for performing exergy analyses (see [18]).

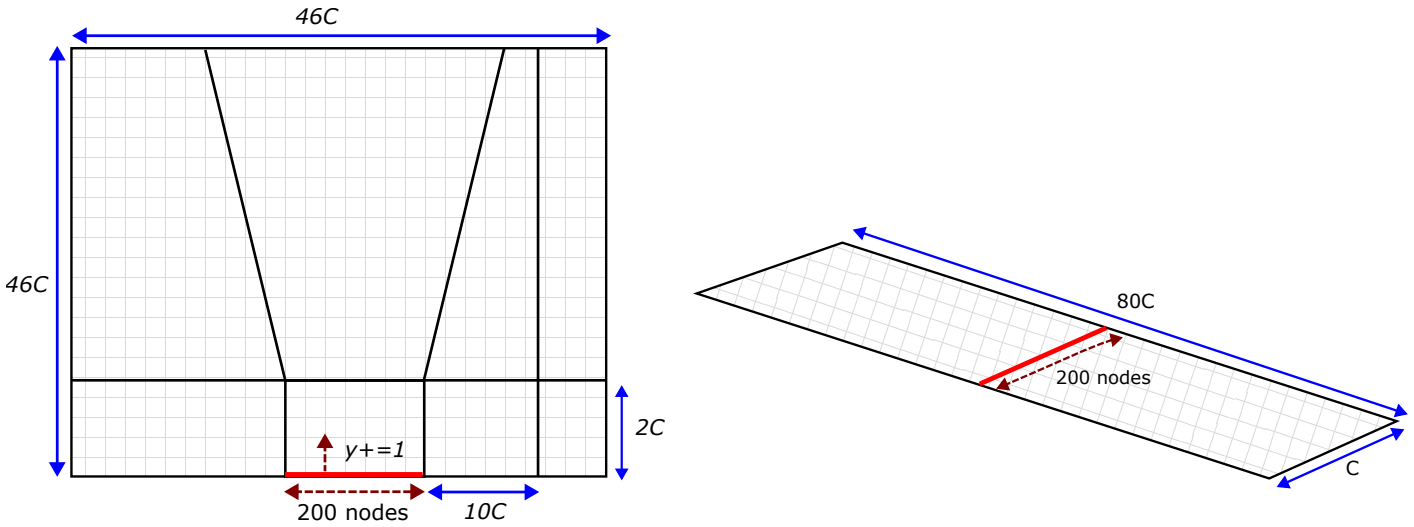



**Fig. 8 Flat plate mesh domain in Fluent (left) and FlightStream (right)**

### B. Data validation

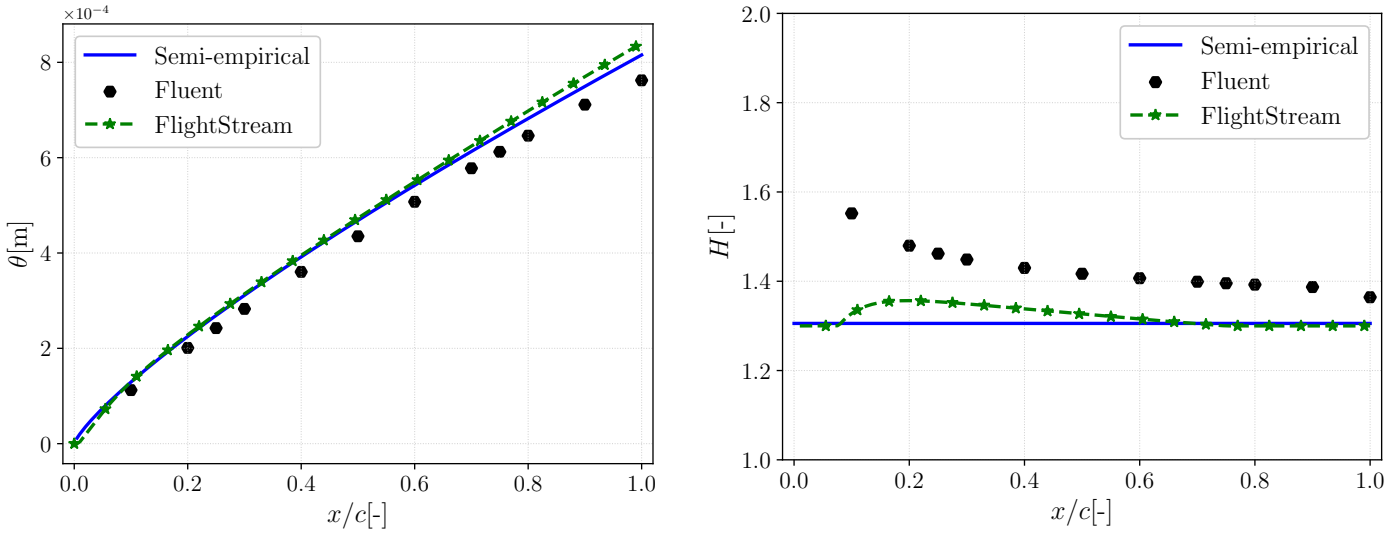
In the flat plate case at zero incidence, the aerodynamic and local boundary layer coordinate systems coincide, so that $u = U$. With no longitudinal pressure gradient, the boundary layer edge velocity remains constant and equal to the freestream velocity, $U_e = u_0$, along the chord.

Semi-empirical expressions exist to describe the well-known flat plate turbulent test case. The velocity profile can be approximated by the $\frac{1}{7}$ power law velocity profile, as shown in Eq.24 (see [19]). The corresponding integral boundary layer parameter relations are presented in Eq.25. The $\frac{1}{7}$ power law is valid only for a turbulent flat plate, whereas the Swafford method is valid for any geometry.

$$\frac{U}{U_e} = \left(\frac{n}{\delta}\right)^{\frac{1}{7}} \tag{24}$$

$$\frac{\delta}{x} = 0.372(Re_x)^{-\frac{1}{5}} \qquad \frac{\delta^*}{x} = 0.047(Re_x)^{-\frac{1}{5}} \qquad \frac{\theta}{x} = 0.036(Re_x)^{-\frac{1}{5}} \qquad H = \frac{\delta^*}{\theta} = 1.306 \tag{25}$$

Integral boundary layer quantities require detailed examination, as they will serve as input data for the low-fidelity equation of $\overline{\dot{E}_u}$ (Eq.20). Fig.9 shows the momentum thickness $\theta$ (left) and the shape factor $H$ (right) from both low and mid-fidelity data, compared with semi-empirical expressions from Eq.25). These parameters are essential because they serve as inputs for the Swafford boundary layer profile reconstruction method, which is required for computing the missing terms of the low-fidelity formulation. For low-fidelity data, these quantities are directly provided as outputs from FlightStream resulting from the viscous coupling. For mid-fidelity data, the profiles $U(n)$ from slices taken at specific locations $x$ have been integrated over $\delta$ to compute $\theta$ and $H$. In Fig.9a, the $\theta$ values from FlightStream show good agreement with the semi-empirical expression, while $\theta$ computed form Fluent is slightly lower.




**(a) Momemtum thickness $\theta$ along the chord** **(b) Shape factor $H = \frac{\delta^*}{\theta}$ along the chord**

**Fig. 9 Boundary layer integral parameters comparison**

In Fig.9b, for the shape factor $H$, FlightStream gives results that are close to the semi-empirical value, with a noticeable deviation in the maximum value of $\Delta H \approx 0.05$ between $x/c = 0.1$ and 0.6. However, a significant deviation in $H$ is observed when calculated from Fluent compared to the semi-empirical value across the entire chord ($\Delta H \approx 0.25$ at $x/c = 0.1$), which decreases to a minimum at the trailing edge, where $\Delta H \approx 0.05$.
The discrepancies between the Fluent and FlightStream solutions and the empirical values could arise from modeling the flat plate as infinitely thin. This can result in disturbances at the leading edge, particularly in the Fluent simulations. Employing a different mesh, where the flat plate is modeled as a very thin airfoil, could provide better results.

Boundary layer velocity profiles at the trailing edge of the flat plate ($x/c$ =1) are shown in Fig.10. The semi-empirical profile (blue curve) is given by the power law of Eq.24. The red curve represents the velocity profile $U(n)$ directly obtained from the Fluent simulations. The remaining curves correspond to boundary layer profiles reconstructed using the Swafford method: the black curve is calculated using $\theta$ and $H$ from Fluent (black curves in Fig.9), while the green curve is calculated using $\theta$ and $H$ from FlightStream (green curves in Fig.9).

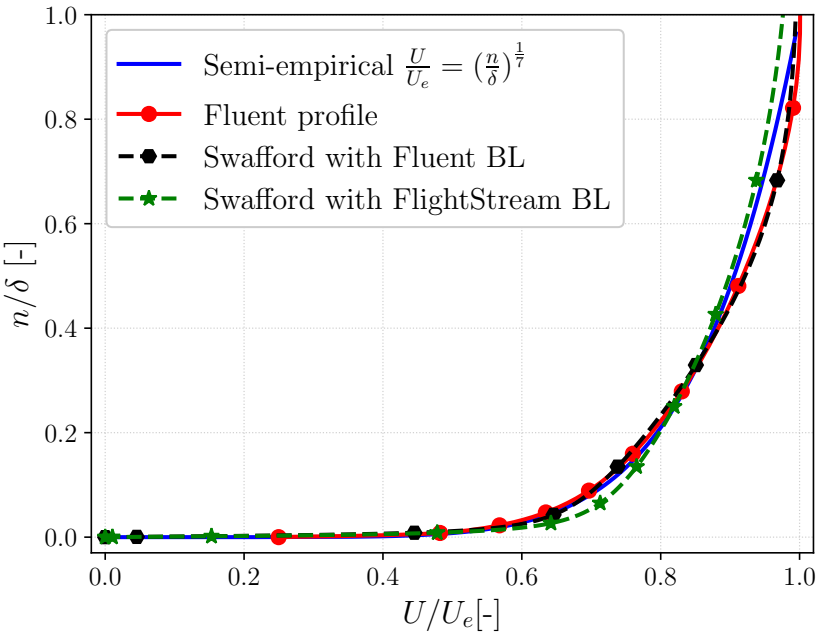



**Fig. 10 Boundary layer (BL) velocity profiles at the end of flat plate ($x/c$=1)**

In Fig.10, there is generally good agreement between the semi-empirical power law profiles and those obtained from low and mid-fidelity data. The profile derived from FlightStream (green) differs from the semi-empirical profile primarily near the wall, whereas the profiles obtained from Fluent show discrepancies in the outer region of the boundary layer. The excellent agreement between the velocity profile directly provided by Fluent (in red) and the profile computed using the Swafford reconstruction method (in black), derived from $\theta$ and $H$ corresponding to the same red curve, validates the accuracy of the Swafford method and justifies its use.

### C. Validation of the low-fidelity formulation

Using only $U_e$, $\delta$, $\theta$ and $H$, which are the integral boundary layer parameters typically obtained from a simulation with the panel method, the boundary layer velocity profile $U(n)$ can be reconstructed using the Swafford method. For the present compressible flat plate case (Mach number=0.3), with adiabatic walls and with $\frac{d|U_e|}{ds}\frac{c}{V_\infty} \approx 0$, Eq.22 is applied to compute $\rho$. All the integral boundary layer $k$, $m$, $K$ and $M$ are then computed, allowing for the evaluation of the recoverable component of the profile drag $\overline{\dot{E}}_u$ through the low-fidelity equation Eq.20. This outlines the calculation chain of the low-fidelity exergy-based formulation.

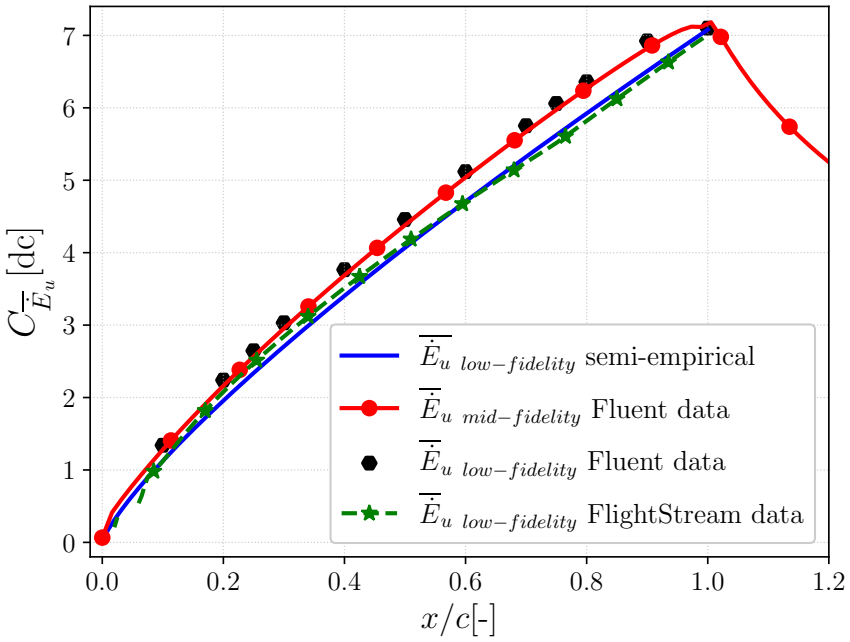



**Fig. 11 Validation of the low-fidelity formulation for $\overline{\dot{E}_u}$ (Eq.20)**

The non-isentropic exergy $\overline{\dot{E}}_u$ non-dimensionalized and expressed in drag count, obtained along the flat plate chord is shown in Fig.11. As a reminder, this represents the amount of energy that can still be recovered and thus it highlights the energy recovery margin. It can be observed that for a flat plate, profile drag can be reduced up to about 7 dc.

The red curve represents $\overline{\dot{E}}_u$ obtained with the mid-fidelity formulation of Aguirre using the RANS data provided by Fluent. This serves as the reference that the low-fidelity formulation aims to approximate. The black dots depict $\overline{\dot{E}}_u$ computed using the low-fidelity formulation in Eq.20. The integral boundary layer parameters $\delta$, $\theta$, $H$, $U_e$ calculated from the Fluent data are used to reconstruct the velocity profile $U(n)$ with the Swafford method. Then $U(n)$ and $\rho(n)$ profiles (the latter computed using Eq.22) are used to compute the integral terms in Eq.20. For the same initial flow-field data from Fluent, the $\overline{\dot{E}}_u$ results from the reference mid-fidelity formulation (red curve) and the low-fidelity formulation (black dots) show excellent agreement, thus validating Eq.20 for the flat plate case.

Furthermore, $\overline{\dot{E}}_u$ corresponding to the low-fidelity formulation with $\delta$, $\theta$, $H$, $U_e$ directly provided by FlightStream coupled with the Swafford reconstruction, exhibits a discrepancy with the low-fidelity $\overline{\dot{E}}_u$ computed from the Fluent data (green curve vs. black dots ). This discrepancy, which is less than 0.5 dc along the flat plate, is primarily due to differences in the integral boundary layer parameters, $\theta$, $H$ provided by Fluent and FlightStream as shown earlier in Fig.9. Thus, the integral boundary layer parameters used as input of the low-fidelity formulation provided by Fluent show notable deviations from the semi-empirical solution. The low-fidelity $\overline{\dot{E}}_u$ curve, calculated from the semi-empirical $\frac{1}{7}$ power law profile, is shown in blue. This, in a way, serves as the semi-empirical reference for low-fidelity exergy. The low-fidelity curve $\overline{\dot{E}}_u$ calculated from the FlightStream data closely matches this semi-empirical curve (green vs blue curve), since the input values of $\theta$ and especially $H$ provided by the FlightStream simulation are much closer to the semi-empirical values than those provided by Fluent. This demonstrates that low-fidelity data can be effectively used for exergy analysis.

## VII. Conclusion

A new exergy-based aerodynamic analysis methodology suited to low-fidelity data has been introduced. The foundation of this methodology lies in the decomposition of exergy into its isentropic and non-isentropic components, following Aguirre's method. The non-isentropic exergy, associated with viscous losses, directly relates to profile drag and is confined to the boundary layer region. An equation for the non-isentropic axial kinetic exergy, $\overline{\dot{E}_u}$ (Eq.20) suited to low-fidelity data, has been derived, expressing $\overline{\dot{E}_u}$ as a function of the boundary layer integral quantities. This equation has been validated through comparison with mid-fidelity exergy formulations for the flat plate in the turbulent regime. The reconstruction method for the turbulent velocity profiles using Swafford method has also been validated. This low-fidelity formulation represents a valuable preliminary design tool for developing aircraft with enhanced fuel efficiency by directly providing a mapping of potential power-saving opportunities on the surface of the studied body. The results of this work open up the scope toward further developments and validations of the low-fidelity exergy formulation for increasingly complex aircraft geometries.

## References


[1] White, F. M., Viscous Fluid Flow, McGraw-Hill, 1991. Google-Books-ID: G6IeAQAAIAAJ.

[2] Standen, N. M., "Calculation of integral parameters of a compressible turbulent boundary layer using a concept of mass entrainment," 1964.

[3] Drela, M., and GILES, M., "Viscous-Inviscid Analysis of Transonic and Low Reynolds Number Airfoils," Aiaa Journal - AIAA J, Vol. 25, 1987, pp. 1347–1355. https://doi.org/10.2514/3.9789.

[4] Ahuja, V., Hartfield, R. J., and Ciliberti, D., "Three-dimensional Viscous Coupling & Flow Separation Enhancements to an Inviscid Surface Vorticity Flow Solver," AIAA SCITECH 2023 Forum, AIAA SciTech Forum, American Institute of Aeronautics and Astronautics, 2023. https://doi.org/10.2514/6.2023-2455, URL https://arc.aiaa.org/doi/10.2514/6.2023-2455.

[5] Drela, M., "Power Balance in Aerodynamic Flows," AIAA Journal, Vol. 47, No. 7, 2009, pp. 1761–1771. https://doi.org/10.2514/1.42409, URL https://arc.aiaa.org/doi/10.2514/1.42409, publisher: American Institute of Aeronautics and Astronautics.

[6] Betz, A., "A method for the direct determination of wing-section drag," , Nov. 1925. URL https://ntrs.nasa.gov/citations/19930090720, nTRS Author Affiliations: NTRS Report/Patent Number: NACA-TM-337 NTRS Document ID: 19930090720 NTRS Research Center: Legacy CDMS (CDMS).

[7] Maskell, E. C., Progress Towards a Method for the Measurement of the Components of the Drag of a Wing of Finite Span, RAE, 1973. Google-Books-ID: vLgsyAEACAAJ.

[8] Katz, J., and Plotkin, A., Low-Speed Aerodynamics, Cambridge University Press, 2001. Google-Books-ID: rAS1DmBRLo8C.

[9] Meheut, "Drag-Breakdown Methods from Wake Measurements," , 2008. https://doi.org/10.2514/1.29051, URL https://www.researchgate.net/publication/245426347_Drag-Breakdown_Methods_from_Wake_Measurements.

[10] Sato, S., "The power balance method For aerodynamic performance assessment," Thesis, Massachusetts Institute of Technology, 2012. URL https://dspace.mit.edu/handle/1721.1/75837, accepted: 2013-01-07T19:05:14Z.

[11] Aguirre, M. A., "Exergetic analysis of innovative aircrafts with aero-propulsive coupling," These de doctorat, Toulouse, ISAE, Feb. 2022. URL https://theses.fr/2022ESAE0008.

[12] Arntz, A., "Civil Aircraft Aero-thermo-propulsive Performance Assessment by an Exergy Analysis of High-fidelity CFD-RANS Flow Solutions," Ph.D. thesis, 2014.

[13] Aguirre, M. A., Duplaa, S., Carbonneau, X., and Turnbull, A., "Velocity Decomposition Method for Exergy-Based Drag Prediction," AIAA Journal, Vol. 58, No. 11, 2020, pp. 4686–4701. https://doi.org/10.2514/1.J059414, URL https://doi.org/10.2514/1.J059414, publisher: American Institute of Aeronautics and Astronautics _eprint: https://doi.org/10.2514/1.J059414.

[14] Drela, M., Flight Vehicle Aerodynamics, 2014. URL https://www.semanticscholar.org/paper/Flight-Vehicle-Aerodynamics-Drela/c5a305cd57ed332285b35a0c7d086348f4409c83.

[15] Whitfield, D. L., "Integral Solution of Compressible Turbulent Boundary Layers Using Improved Velocity Profiles," 1978.

[16] Coles, D., "The law of the wake in the turbulent boundary layer," Journal of Fluid Mechanics, Vol. 1, No. 2, 1956, pp. 191–226. https://doi.org/10.1017/S0022112056000135, URL https://www.cambridge.org/core/product/identifier/S0022112056000135/type/journal_article.

[17] Swafford, T. W., "Analytical approximation of two-dimensional separated turbulent boundary-layer velocity profiles," AIAA Journal, Vol. 21, No. 6, 1983, pp. 923–926. https://doi.org/10.2514/3.8177, URL https://arc.aiaa.org/doi/10.2514/3.8177.

[18] Angel, A. M., and Sébastien, D., "Epsilon v3: exergy-based aerodynamic analysis tool for cfd and wtt data," 2022. URL https://openscience.isae-supaero.fr/Default/doc/SYRACUSE/5879/epsilon-v3-exergy-based-aerodynamic-analysis-tool-for-cfd-and-wtt-data.

[19] Schlichting, H., and Gersten, K., Boundary-Layer Theory, Springer, Berlin, Heidelberg, 1979. https://doi.org/10.1007/978-3-662-52919-5, URL http://link.springer.com/10.1007/978-3-662-52919-5.